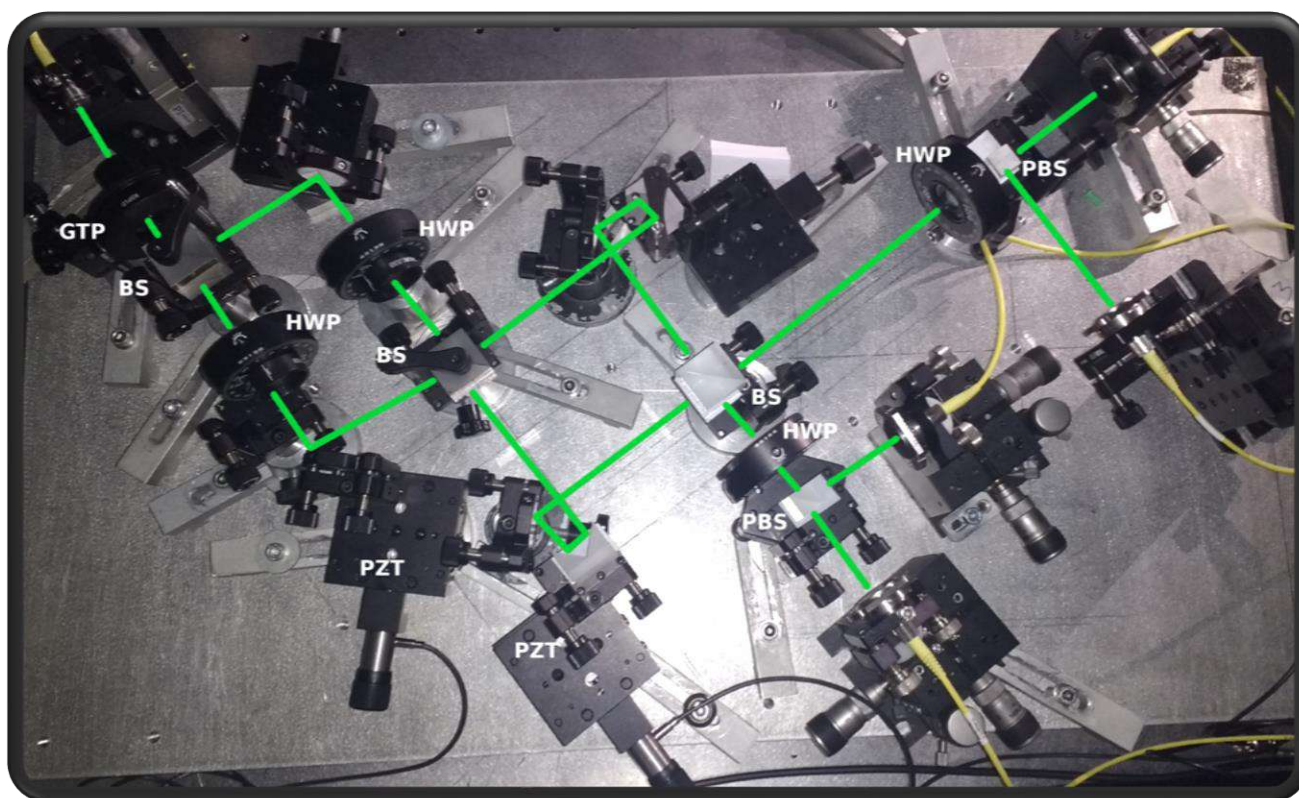




# NANOSCIENCE LABORATORY

## HIGHLIGHTS 2018



*Image on the front cover:*  
The set-up used to measure single particle entanglement.  
Photo by M. Pasini

## NANOSCIENCE LABORATORY

### MEMBERS (2018)

#### Faculty staff

Lorenzo Pavesi (full professor, head)  
 Marina Scarpa (full professor)  
 Zeno Gaburro (associate professor)  
 Paolo Bettotti (associate professor)  
 Enver Sangineto (researcher)

#### Technical staff

Enrico Moser  
 Giorgio Fontana (EP7 level)

#### Administrative staff

Tatsiana Egorova

#### Post-doctoral fellows

Pierre Guilleme  
 Massimo Borghi (left april, 2018)

#### Doctoral students

Tatevik Chalyan (left july 2018)  
 Alessandro Trenti (left april 2018)  
 Claudio Castellan  
 Cecilia Ada Maestri  
 Chiara Piotto  
 Stefano Signorini  
 Sara Piccione  
 Stefano Biasi  
 Chiara Vecchi  
 Clara Zaccaria  
 Davide Bazzanella  
 Nicolò Leone  
 Astghik Chalyan (visiting PhD student, left february 2018)

#### Master students

Riccardo Franchi  
 Damiano Lodi  
 Andrea Volpini  
 Mattia Finazzer  
 Matteo Pasini  
 Giovanni Donati

## SCIENTIFIC MISSION

### Introduction to the Nanoscience Laboratory

The Nanoscience Laboratory (NL) is one of the scientific groups of the Department of Physics, University of Trento. Its main areas of research are neuromorphic photonics, integrated quantum photonics, linear and nonlinear silicon photonics and nanobiotechnologies. The mission of NL is to generate new knowledge, to develop understanding and to spin-off applications from physical phenomena associated with photons and their interactions with matter, particularly when it is nanostructured. In particular, NL aims at understanding the optical properties of lightwave systems such as optical waveguides, microresonators and complex dielectric systems. NL covers the whole food chain from fundamental phenomena to device applications, where the photonic platform is compatible with the main driving silicon microelectronic technologies. However, silicon is not the only material studied. Other fields of interest concern the use of cellulose to tailor the properties of nanostructure atom-by-atom or the use of perovskites to investigate their new properties.

NL research group consists of more than 25 people with different scientific backgrounds. Researchers from physics, physiology, bio-chemistry, materials science and electrical engineering are gathered to form a group of interdisciplinary nature. It is worth mentioning that NL collaborates

closely with the Center of Materials and Microsystems, Fondazione Bruno Kessler (FBK). This collaboration spans over the last thirty years and covers such topics as fabrication, testing and application of biomaterials and silicon based devices. Both participate in many common projects. The current ones are: projects LESSO, NEMO and QRANGE. A new tight collaboration is ongoing with the Trento units of CNR-INO, specifically dedicated to implement quantum optics in integrated chip. Moreover, with the support of FBK and CNR and every odd year, NL organizes a winter school on optoelectronics and photonics. In 2019, the 10<sup>th</sup> edition is organized on “Non-linear Photonics” (20-26 January, 2019). Furthermore, the members of NL are often invited to participate in the organizing committees of international conferences or workshops.

The research activities of NL are mainly supported by the local government (PAT), by the European Commission, by the Italian Ministry of Education, University and Research (MIUR) and by companies. During the period covered by these Highlights, NL has been and is involved in the following projects: project PRIN-MIUR NEMO “Nonlinear dynamics of optical frequency combs”, some European projects within the 7th Framework: SYMPHONY (FP7-ICT-2013-10) and “Integrated Reconfigurable silicon phonic Switch – IRIS” (FP7-ICT-2013-11), ERC Advanced Grant project: “Unveiling the relationship between brain connectivity and function by integrated photonics – BACKUP (ERC-2017-ADG-788793)”, QRANGE (H2020-

FETFLAG-2018-03): “Quantum Random Number Generators: cheaper, faster and more secure”; Q@TN project “Quantum Science and Technology in Trento”, India-Trento Program for Advanced Research - ITPAR: “A cheap, light, compact source for QKD based on intraparticle entanglement in an integrated photonic circuit”, LESSO (ASI “Nuove idee per la componentistica spaziale del futuro - TRL”): “Laser etero-integrato a stato solido per trappole ottiche”, NANOFARM (Legge Provinciale 13 dicembre, 1999 n. 6).

### Silicon Nanophotonics

Silicon photonics is the technology where photonic devices are produced by standard microelectronic processes using the same paradigm of electronics: integration of a large number of devices to yield a high circuit complexity, which allows for high performances and low costs. Here, the truth is to develop photonic devices that can be easily integrated to improve the single device performance and to allow high volume production.

In the next year we will mostly concentrate on two alternative approaches where photonics is used to compute. On one side we will develop new scheme to implement artificial intelligence in a photonic silicon chip by using neuromorphic computing schemes. On the other side, we will use silicon photonics to provide a suitable platform for quantum computing and quantum simulations. In both approaches the fundamental device is the silicon microresonator where whispering gallery modes induce nonlinearities which can be exploited to generate new quantum states of light or to realize recurrent neural network. In addition, we use microdisks or micro-rings to study new physics (chirality, frequency comb generation, entangled photon generation). The microresonators are coupled directly with narrow mode SOI (Silicon-on-Insulator) waveguides. High quality factor cavities allow studying fundamental quantum optics concept such Bogoliubov excitation in quantum fluid of light or entangled photon generation.

To develop silicon photonics, one further add-on is making silicon to do something that it is not able to do in its standard (bulk) form. Low dimensional silicon, where small silicon nanocrystals or nanoclusters (Si-nc) are developed, is one way to compel silicon to act as an active optical material. Alternatively, we use the built-in or p-i-n induced electric fields to tune the non-linear optical properties of silicon waveguides for the development of new MIR sources (parametric generation via second order effects or frequency comb generation). Nonlinear optics is used to generate pairs of entangled photons, which in turn feed quantum interferometers or integrated quantum photonic circuits.

### Nanobiotechnologies, antioxidants and human health

All the aspects related to the nano-bio interfaces (which are the structures where the co-existence of physical principles and biological molecules is clearly evident) are a challenging field of research. Though the leading research concerns

the design, synthesis and dynamic behavior of nano-structured bio-interfaces, more specifically we are working on three research topics: silicon- and titanium based nanosystems, single molecule detection, and antioxidant behavior in micelle systems, polymers and nanoporous structures.

To develop silicon based bio-sensors, we are currently focused on silicon based hybrid nanostructures. In particular silicon or silicon nitride flat or porous films are the starting inorganic support into which bio active layers are designed. Biological recognition elements are introduced on this hybrid layer. Molecular surface density, active layer thickness and integration of the bio-active interface with photonic devices will be the future challenges to develop the sensor system. In addition, we are developing nanostructured hybrid interfaces to capture bio-analytes and enhance their Raman signals. Gold and silver nanoparticles are used as enhancers. Beyond traditional sensor applications, silicon nanostructures can be used as “nanosensors”, which monitor the intracellular events without introducing irreversible perturbations. To this regard light emitting silicon quantum dots appear very promising. We are studying the nanoparticle coating to increase optical stability and decrease toxicity, moreover conjugation to biological molecules and strategies to increase cell uptake and control intracellular localization are future steps of this research. Titanium nanotubes showing hydroxyl-rich interfaces have been synthesized. These nanosystems are easily dispersed and stable in aqueous solutions and show a high photocatalytic activity.

### Experimental facilities

The NL facilities allow for detailed experimental studies in nanoscience, photonics and biotechnologies. Since the effective collaboration with FBK most material processing and device productions are performed within their premises. For photonics, we have facilities to cover the light spectrum from the THz to UV ranges with whatever time resolution is needed. Laser sources comprehends: Ti-sapphire fs-ps laser (1 W average over 1000-700 nm, 2 ps or 70 fs pulses, 82 MHz repetition rate) interfaced with a second harmonic generator and pulse picker; TOPAS pumped with an amplified Ti:Sa laser which covers the 1-2.6  $\mu\text{m}$  range with 35 fs, 10 kHz, 3 mJ; 2W tunable CW Cr:ZnSe/S fiber-bulk hybrid laser to cover the 2-3  $\mu\text{m}$  range; three tunable CW lasers (850-870 nm, 1200 - 1700 nm and 1500 - 1600nm) fiber pig-tailed; high power fiber-laser at 1550 nm (1-100 MHz, 50 ps); 4W EDFA and 2W semiconductor amplifiers, several pig-tailed diode lasers, ASE source at 1550 nm and a broad band SLD at 800 nm; three high-power true-CW DPSS single-line laser operating at 532, 473 and 355 nm. Detectors comprehend: visible and infrared photomultipliers and CCDs, a streak camera with ps resolution, 4K cooled bolometers which cover THz region, avalanche photodiodes for vis and IR ranges plus single photon detectors in the visible and IR. Two home-made MIR single photo counters. To perform spectral analysis several set-ups are available: FTIR and dispersive spectrophotometers, a micro-Raman setup, a micro-FTIR and a UV-vis-IR spectrophotometer (shared with other laboratories), UV-Vis and fluorescence

spectrophotometer dedicated to biochemical experiments. Seven set-ups are dedicated to the characterization of waveguides equipped with nanopositioning systems and polarization controllers, each specified on a given function: visible, quantum, passive infrared, non-linear infrared, non-linear MIR and on wafer. Other devices are: - a solar simulator for cells up to 5 inches in size; - two nanoprobe stations (AFM and SNOM) - two semiconductor probe stations (4 and 8 inches) and different electrical characterization systems (I-V, Z- $\Omega$ , EL-I, etc.). Four-channels 16GHz oscilloscopes. Two VIS to NIR optical spectrum analyzers are available. A probe station is interfaced with a fibres bundle to a spectrometer interfaced with visible IR and CCDs cooled with liquid nitrogen. An electrochemical laboratory with various chemical hoods, galvanostats and volt-ameters is available for sample processing. For optical, electrical and molecular dynamics simulations, the laboratory uses free and commercial software and has a work-station with 4 GPU. Two laboratories are also available, one dedicated to chemical synthesis and the other to the preparation of biological samples. As part of the ERC-BACKUP project, two other laboratories with biological hoods, incubators and confocal microscopes have been set up. In one, a confocal microscope with an insert for electrophysiology and optogenetics measurement equipped with a "spinning disk" system for fast acquisitions and a super-resolution system. While a 20 Gbps optical measurement system with arbitrary 20 GHz signal generator, electro-optical modulators, coherent detectors and 20 GHz oscilloscopes is currently being purchased.

### 2018 publications

- C. Castellan, A. Chalyan, M. Mancinelli, P. Guilleme, M. Borghi, F. Bosia, N.M. Pugno, M. Bernard, M. Ghulinyan, G. Pucker and L. Pavesi "Tuning the strain-induced resonance shift in silicon racetrack resonators by their orientation", *Optics Express* 26, 4204-4218 (2018).
- A. Trenti, M. Borghi, S. Biasi, M. Ghulinyan, F. Ramiro-Manzano, G. Pucker, and L. Pavesi "Thermo-optic coefficient and nonlinear refractive index of silicon oxynitride waveguides", *AIP Advances* 8, 025311 (2018).
- Z. Bisadi, F. Acerbi, G. Fontana, N. Zorzi, C. Piemonte, G. Pucker and L. Pavesi "Compact Quantum Random Number Generator with Silicon Nanocrystals Light Emitting Device Coupled to a Silicon Photomultiplier", *Frontiers in Physics: Optics & Photonics* 6:9.doi: 10.3389/fphy.2018.00009 (2018).
- S. Piccione, M. Mancinelli, A. Trenti, G. Fontana, J. Dam, et al. "Mid-infrared coincidence measurements based on intracavity frequency conversion", *Proc. SPIE 10516, Nonlinear Frequency Generation and Conversion: Materials and Devices XVII*; 105161P (2018).
- N. Zecevic, M. Hofbauer, B. Goll, H. Zimmermann, S. Tondini, A. Chalyan, G. Fontana, L. Pavesi, F. Testa, S. Stracca, A. Bianchi, C. Manganelli, P. Velha, P. Pintus, C. Oton, C. Kopp, L. Adelmini, O. Lemonnier, G. Pares, G. Chiaretti, A. Serrano, J. Á. Ayucar, G. Battista Preve, M.-S. Kim, and J. Moo Lee "A 3D Photonic-Electronic Integrated Transponder Aggregator With 48  $\times$  16 Heater Control Cells", *IEEE Photonics Technology Letters* 30, 681-684 (2018).
- I. Suárez, E. Hassanabadi, A. Maulu, N. Carlino, C. A. Maestri, M. Latifi, P. Bettotti, I. Mora-Seró, J. P. Martínez-Pastor "Integrated Optical Amplifier-Photodetector on a Wearable Nanocellulose Substrate", *Advanced Optical Materials*, vol. 6, issue 12 (2018).
- F. Acerbi, Z. Bisadi, G. Fontana, N. Zorzi, C. Piemonte and L. Pavesi "A Robust Quantum Random Number Generator Based on an Integrated Emitter-Photodetector Structure", *IEEE Journal of Selected Topics in Quantum Electronics* 24, 6101107 (2018).
- E. Chiste, A. Ghafarinazari, M. Donini, V. Cremers, J. Dendooven, C. Detavernier, D. Benati, M. Scarpa, S. Dusi and N. Daldosso "TiO<sub>2</sub>-coated luminescent porous silicon microparticles as a promising system for nanomedicine", *Journal of Materials Chemistry B*, 6, 1815-1824 (2018).
- P. Bettotti, V. Visone, L. Lunelli, G. Perugino, M. Ciaramella, A. Valenti "Structure and Properties of DNA Molecules Over The Full Range of Biologically Relevant Supercoiling States", *Scientific Reports*, 8, 6163 (2018).
- C. Castellan, S. Tondini, M. Mancinelli, C. Kopp and L. Pavesi "Low crosstalk silicon arrayed waveguide gratings for on-chip optical multiplexing", *Proc. SPIE 10686, Silicon Photonics: From Fundamental Research to Manufacturing*; 106860V (2018).
- T. Toccoli, P. Bettotti, A. Cassinese, S. Gottardi, Y. Kubozono, M. Antonietta Loi, M. Manca and R. Verucchi "Photophysics of Pentacene-Doped Picene Thin Films", *J. Phys. Chem. C: Plasmonics; Optical, Magnetic, and Hybrid Materials* 122, 16879-16886 (2018).

- S. Signorini, M. Mancinelli, M. Borghi, M. Bernard, M. Ghulinyan, G. Pucker and L. Pavesi “Intermodal four-wave mixing in silicon waveguides”, *Photonics Research* 6, 805-814 (2018).
- F. Khozaymeh, M. Razaghi, T. Chalyan and L. Pavesi “Fast analytical modelling of an SOI micro-ring resonator for bio-sensing application”, *Journal of Physics D: Applied Physics* 51, 285401 (2018).
- S. Signorini, S. Piccione, M. Ghulinyan, G. Pucker, L. Pavesi “Are on-chip heralded single photon sources possible by intermodal four wave mixing in silicon waveguides?”, *Proc. of SPIE Vol. 10733* (2018).
- R. Checchetto, P. Bettotti, R. Sennen Brusa, G. Carotenuto, W. Egger, C. Hugenschmidt and A. Miotello “Anomalous molecular infiltration in graphene laminates”, *Phys. Chem. Chem. Phys.* 20, 24671-24680 (2018).
- F. Turri, S. Biasi, F. Ramiro Manzano, L. Pavesi “A Free-Space Interferometer for Phase-Delay Measurements in Integrated Optical Devices in Degenerate Pump-and-Probe Experiments”, *IEEE Transactions on Instrumentation and Measurement*, vol. 67, no.12, 2863-2871 (2018)

#### 2018 PhD Thesis:

1. Alessandro Trenti “*Generation, manipulation and detection of NIR and MIR entangled photon pairs*” (20<sup>th</sup> April, 2018)
2. Tatevik Chalyan “*Optical biosensors for mycotoxin detection in milk*” (18<sup>th</sup> July, 2018)

## 1. Single-Photon Interferometry for Bell Inequality Measurements (Matteo Pasini, Nicolò Leone)

Photons are the main platform for quantum communication and cryptography applications: photonic schemes for Quantum Key Distribution (QKD) and Quantum Random Number Generation (QRNG) have been largely demonstrated. The development of quantum gates for the manipulation of qubit states and the detection of entanglement are two fundamental building blocks in many of these schemes. Among the possible tests for entanglement, the most used is the Bell Inequality. It was historically introduced to provide an experimental answer to the famous Einstein’s paradox of a “spooky action at a distance”. By measuring the probability of the quantum system to be projected in a definite state after the detection, we can compute a Bell parameter with a numerical bound predicted by classical theories. An experimental violation of this inequality is a signature of the quantum features of the system, and is widely used as an entanglement test. Performing a Bell test, however, requires a precise control of the degrees of freedom used as qubits.

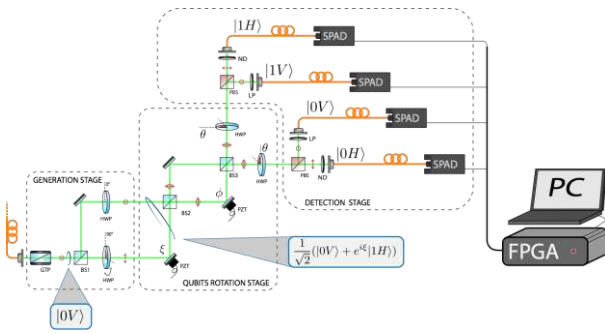


Figure 1: Schematic of the experimental setup.

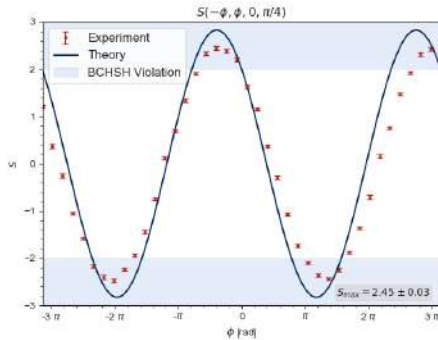


Figure 2: Plot of the Bell parameter  $S$ , showing a violation of the Bell Inequality using a WCS.

Recently, a new kind of entanglement is being studied to improve existing protocols and design new ones: hyperentangled states are quantum states where entanglement is present between many degrees of freedom belonging to the same particle. We consider single photons in a hyperentangled state of momentum (spatial direction of propagation, at fixed frequency) and polarization. A setup (Fig. 1) composed of two cascaded free-space Mach Zehnder Interferometers (MZI), with waveplates for polarization control, allows the state generation and the manipulation of the two

qubits. Indeed, MZIs allow to control the superposition of momentum states, acting as universal quantum gates. However, free space single-photon interferometers are very sensible to noise and imperfections. The setup has been carefully stabilized and characterized and, performing suitable transformations on the photon quantum state, we have computed and measured the Bell Inequality. By using a source of Weak Coherent States (WCS), we have witnessed a violation of the inequality (Fig. 2), which indicates the quantum nature of the correlations between the involved degrees of freedom.

The use of single photon hyperentangled states could allow the self-certification of existing QKD and QRNG protocols, assuring that they operate in a quantum regime, as well as new ways of transferring information in a secure way.

## 2. Bogoliubov set-up limits and potentialities (Nicolò Leone, Stefano Biasi)

A new way to study the superfluid nature of light consists in the observation of the spatial evolution of a signal wave in a degenerate four wave mixing process under the approximation of dominant pump intensity. Within a mathematical analogy, the equations that describe this process are identical to the Bogoliubov formulation of the Gross-Pitaevskii equation, where a small fluctuation propagates over the ground state of a dilute Bose-Einstein condensate.

Within this analogy, the pump wave is considered the ground state, while the signal acts as the perturbation. When the  $\text{Sign}[\beta_2] = \text{Sign}[\gamma]$ , where  $\beta_2$  is the group velocity dispersion of the waveguide and  $\gamma$  is the nonlinear index, the signal evolution is stable against the formation of modulation instabilities due to the nonlinearity. In particular, the phase acquired during the propagation by the signal exhibits a peculiar staircase behavior, when the frequency detuning from the pump wavelength is  $\Delta\omega \approx 0$ . This is in contrast with the usual particle-like parabolic behavior ( $\Delta\phi = \beta_2/2 \Delta\omega^2$  when  $\gamma = 0$ ). The staircase behavior is the evidence of the superfluid nature of light, where the photons behave as a wave of matter and not as single particles. In order to observe this peculiar feature, we have performed phase measurements with a free space Mach Zehnder interferometer (MZI). The setup has a phase stability over time of  $0.08^\circ/\text{min}$  and the acquisition accuracy is  $\delta\phi = \pm 0.05^\circ$  thanks to the introduction of two free space delay lines. The scheme of the MZI is visible in fig. 3.

Unfortunately, the effect induced by the nonlinearity is too small in the waveguide sample of silicon oxynitride and silicon nitride, while in the silicon sample it is totally spoiled by the high linear losses and the presence of two photon absorption and free carrier absorption, that limit the coupled pump power in the waveguide, at the working wavelength of  $1.55\mu\text{m}$ . The butt coupling used to inject the light into the sample induces also a Fabry-Perot oscillation, introducing another source of noise in the experiment. On the other hand, finding new sample could be an option: chalcogenide waveguide and optical fibers are the most interesting platform up to now, in which simulations have revealed encouraging results. While the latter allows increasing the length of the sample to kilometers thank to its low linear losses,

resulting in an increment of the accumulated phase, the first has a nonlinear refractive index similar to the one of silicon, without the presence of nonlinear losses.

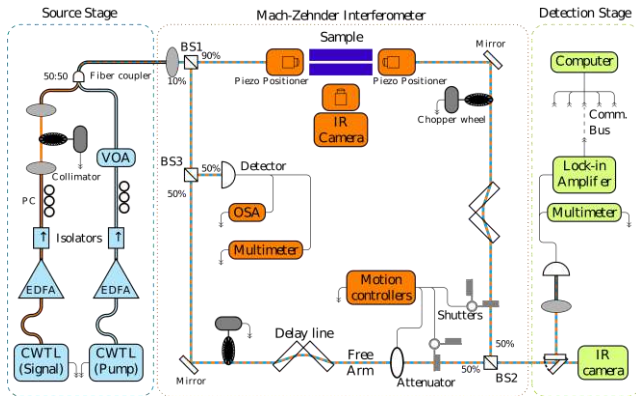


**Figure 3:** Schematic diagram of the experimental setup: the source stage is circled with a blue dotted line, the free space MZI is circled with an orange dotted line while the detection stage is circled with a green dotted line. Probe line is represented in orange, while pump line is represented in blue. Note that connections with bold edges represent optical fibers, while ones with no edges represent free space connections. Black connections are electrical wires. Grey ellipses are collimators.

### 3. The physics of SHG in strained silicon (Chiara Vecchi, Claudio Castellan, Alessandro Trenti)

In order to understand the origin of second order nonlinear effect, we studied second harmonic generation (SHG) in strained silicon waveguides with a  $\text{Si}_3\text{N}_4$  stressing layer. By optical pumping a strained waveguide, we found that the second order nonlinear coefficient  $\chi^{(2)}$  is 0.5 pm/V.

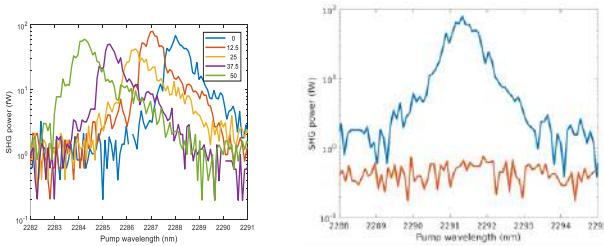


**Figure 4:** (a) SHG power vs pump wavelength for five different values of the applied external strain. The shift of the peak is due to the photoelastic effect. (b) SHG power vs pump wavelength before (blue curve) and after (red curve) the exposition to UV radiation.

This value is different from what other researchers found. Few reports indicated that different stressing layers induce different second order nonlinearities. Therefore, we decided to perform measurements under a controlled strain which is applied via a plastic deformation of the waveguide in a dedicated set-up. The results of a measurement where the strain in the waveguide is increased is shown in Fig. 4(b): a shift of the peak is observed but not an increase of the SHG. The shift is explained by the variation of the refractive index of the waveguide due to the photoelastic effect. What is here

surprising is the lack of the generation efficiency increase. Thus we look for another candidate for the not-negligible  $\chi^{(2)}$ . It is well known that during the deposition of silicon nitride on silicon, there is the formation of charged interface states due to the dangling bonds at the interface. These charged states cause a DC field in the waveguide that interacts with the third order nonlinearity  $\chi^{(3)}$  of silicon and causes a dressed  $\chi^{(2)} = 3\chi^{(3)}E_{DC}$ . It was shown that UV exposition neutralizes the interface state which removes the DC field in the waveguide. SHG measurements after 23 hours UV exposure are shown in Fig. 4(b). It is observed that after the UV exposition no more SHG peak is present. Together with the independence on the applied strain, this demonstrates that the SHG is not due to the strain induced by the stressing  $\text{Si}_3\text{N}_4$  layer, but it is caused by the charges at the interface of the waveguide via the induced electric field.

### 4. Robust geometries for SHG in Si microrings cladded by silicon nitride (Pierre Guilleme, Chiara Vecchi)

In the scope of the Nemo project devoted to quadratic optical frequency combs, geometries for an efficient second-harmonic generation were investigated.

To take advantage of the power enhancement due to the confinement and resonances, we study SHG in a Si microring (Fig. 5). We assume a non-zero  $\chi_{zxy}^{(2)}$  induced by a 140 nm thick  $\text{Si}_3\text{N}_4$  cladding. The waveguide width in the microring is  $w$ , its thickness is  $e$  and the internal microring radius  $R_{in}$ . The fundamental field (pump of wavelength  $\lambda_f$ ) is coupled to the microring by a straight bus waveguide which is also used to collect the SH field (wavelength  $\lambda_{SH}$ ).

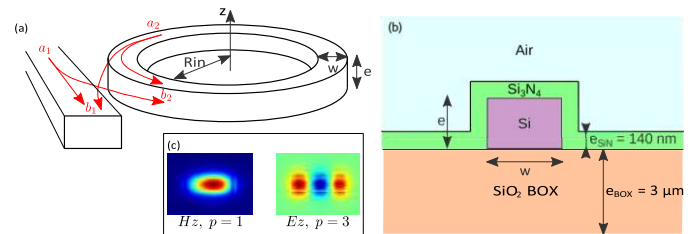
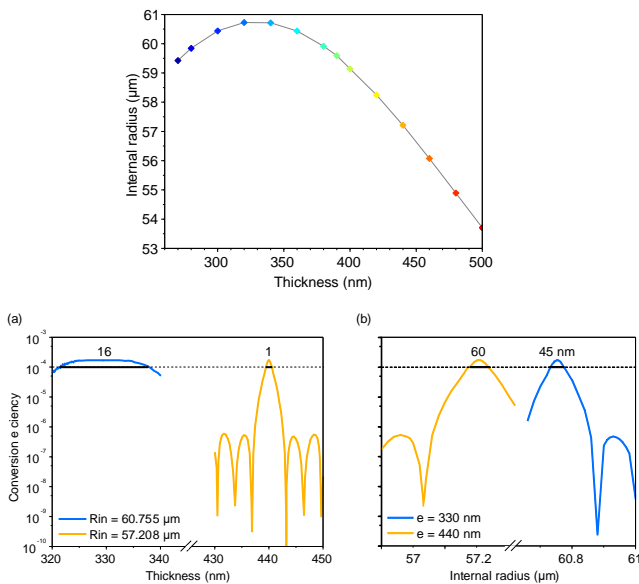


**Figure 5:** (a) System and notations used for the SHG study. (b) Cross section of the microring showing the materials and thicknesses. (c) Mode profiles of a TE mode with radial number  $p = 1$  and TM mode with radial number  $p = 3$

Optimization of the microring design as a function of the waveguide and ring parameters allows determining the dependence of the ring radius on the waveguide thickness which yields phase matching and resonance of both the fundamental and the second harmonic waves. As shown in Fig. 6, the function  $R_{in} = f(e)$  has a flat maximum at  $e = 330$  nm, so the required microring geometry to make SHG at these thicknesses has a range of radii values instead of a fixed radius value. From a practical point of view, this means that we can tolerate variations of  $\pm 10$  nm in the thickness about

the selected value of 330 nm or of the radius about the selected values of 60.755  $\mu\text{m}$  without compromise the generation efficiency. Therefore, the proposed geometry is robust with respect to fabrication tolerances.

In order to illustrate the interest of this robust geometry, we have computed the conversion efficiency  $\eta$ , defined as the power ratio between the generated SH and the pump, both estimated inside the bus waveguide. This evaluation was performed for two different internal radii: i)  $R_{in} = 60.755 \mu\text{m}$  and ii)  $R_{in} = 57.208 \mu\text{m}$ . To simulate a fabrication error, the thickness is swept around the nominal value,  $e = 330 \text{ nm}$  in the first case and  $e = 440 \text{ nm}$  in the second one. The results are shown in Fig. 6(a). In both cases,  $\eta_{max} \approx 1.7 \times 10^{-4}$  when the thickness has the optimum value which yields the optimum microring radius. For the robust geometry (blue line), the SHG remains efficient even when the thickness differs by 10 nm from the optimum value, whereas for the other geometry (orange line)  $\eta$  decreases by at least two orders of magnitude when the thickness differs from the optimum value. In the first case,  $\eta$  is larger than  $10^{-4}$  on a thickness range spanning more than 15 nm while the range is as narrow as 1 nm in the second case.



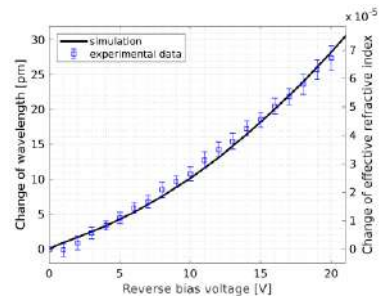
**Figure 6:** (top) Internal radii values that fulfil the criteria of SHG with high efficiency as a function of the waveguide thickness for a silicon microring of width  $w = 800 \text{ nm}$  and a fundamental azimuthal number  $mf = 400$ . (bottom) SHG conversion efficiency  $\eta$  as a function of (a) an error on the thickness  $e$  and (b) an error on the internal radius  $R_{in}$ . The blue line corresponds to  $R_{in} = 60.755 \mu\text{m}$  and  $e = 330 \text{ nm}$ . The orange line corresponds to  $R_{in} = 57.208 \mu\text{m}$  and  $e = 440 \text{ nm}$ . The waveguide width is  $w = 800 \text{ nm}$  and the pump power  $P_{in} = 1 \text{ W}$ . The green lines indicate the range for which  $\eta > 10^{-4}$ .

Fig. 6(b) shows the same kind of study when the internal radius is swept while the thickness is fixed to i)  $e = 330 \text{ nm}$  in the case of the robust geometry and ii)  $e = 440 \text{ nm}$  in the other case. We can see that a fabrication deviation on the radius is not as critical as the one on the thickness since in both cases a 45 nm-deviation on  $R_{in}$  keeps the conversion efficiency larger than  $10^{-4}$ .

## 5. Direct-current Kerr and plasma-dispersion effects in micro-resonators (Riccardo Franchi, Claudio Castellan)

Nowadays, electro-optical modulators are widely used devices in various applications, which range from optical communications to quantum optics. For this reason, it is necessary to make these devices faster and more performing as well as integrated. Compared to other methods, such as the thermo-optical effect or plasma dispersion, non-linear effects can provide a higher modulation speed. A non-linear process widely used to make electro-optical modulators is the Pockels effect but, being a second order non-linear effect, it is possible only if  $\chi^{(2)} \neq 0$ . Silicon is a centrosymmetric material, and so it has  $\chi^{(2)} = 0$ . Therefore, to use this material, its centrosymmetry must be broken. This can be done by stressing silicon: a  $\chi_{\text{cxy}}^{(2)} = (-1.8 \pm 0.2) \frac{\text{pm}}{\text{V}}$  has been recently measured [1]. Another way to make an electro-optical modulator is to use the direct-current Kerr effect, which is a third order non-linear effect. To apply a strong electric field inside the silicon waveguide, lateral p-i-n junctions can be used [2].

We studied the direct-current Kerr and plasma-dispersion effects in resonators with lateral p-i-n junctions. The study is performed both from an experimental and a simulative point of view. First, we measured the IV characterization of the p-i-n junctions. Then, we measured the field-induced refractive index variation in silicon microrings where pn junctions have been realized, see Fig. 7.



**Figure 7:** Change of resonant wavelength and effective mode index as a function of reverse bias voltage

Using simulations, we modelled the refractive index variation due to the applied reverse bias voltage. In addition, we estimate an equivalent  $\chi_{\text{eq}}^{(2)} \approx 10 \frac{\text{pm}}{\text{V}}$  for our devices. Compared to the strained-silicon platform, this method yields higher nonlinearities and offers interesting perspectives for the realization of high-speed integrated electro-optic modulators in silicon.

## References

- [1] M. Berciano, et al., “Fast linear electro-optic effect in a centrosymmetric semiconductor”, *Communications Physics* 1, 64 (2018).
- [2] E. Timurdogan, et al., “Electric field-induced second-order nonlinear optical effects in silicon waveguides”, *Nature Photonics* 11.3, 200 (2017).

## 6. Field-induced second harmonic generation in silicon waveguides with lateral doping (Claudio Castellani, Riccardo Franchi)

Due to its centrosymmetric crystal, second order nonlinearities are inhibited in bulk silicon. Therefore, a great effort has been spent in recent years to overcome this limit. An interesting way to do so relies on the application of strong DC fields across a waveguide through a junction, which can enable the Electric-Field-Induced Second Harmonic Generation (EFISH). This is a third order nonlinear process where a pump wave couples with the DC field and generates a second-harmonic wave through an effective second order nonlinear coefficient  $\chi_{\text{eff}}^{(2)} = 3\chi^{(3)}E_{\text{DC}}$ . Here we have fabricated waveguides where lateral junctions were disposed periodically along the waveguide propagation direction to induce a quasi-phase-matched nonlinear process. We used a design, where the electric field induced  $\chi_{\text{eff}}^{(2)}$  changes periodically its sign along the waveguide propagation direction. In this way, the strength of the nonlinear conversion is increased by about one order of magnitude with respect to another geometry where the junctions have all the same polarities. The experimental characterization of the EFISH process confirms the predictions of simulations. Fig. 8 shows the dependence of the generated signal on the bias voltage applied to the p-n junction. This proves that, using this method, it is possible to have a tunable  $\chi_{\text{eff}}^{(2)}$  inside the waveguide

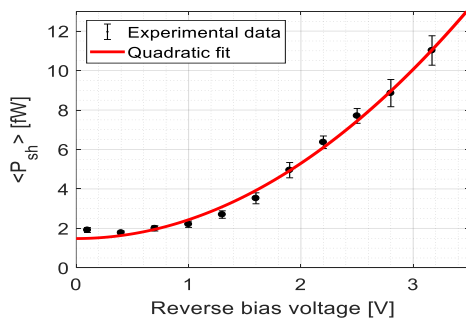


**Figure 8:** Second harmonic power as a function of the reverse bias voltage applied to the p-n junction. Note the low voltage values.

## 7. Four wave mixing control in a photonic molecule made by silicon microring resonators (Massimo Borghi, Alessandro Trenti)

Photonic molecules can be obtained by coupled resonant units, where light propagates in super-modes, analogous to molecular orbitals in atomic systems. They have been demonstrated to be versatile tools in a large number of applications, for instance: dispersion compensation, higher-order filters, gain induced spontaneous symmetry breaking and, most recently, as electronically programmable devices for light trapping and storage [1].

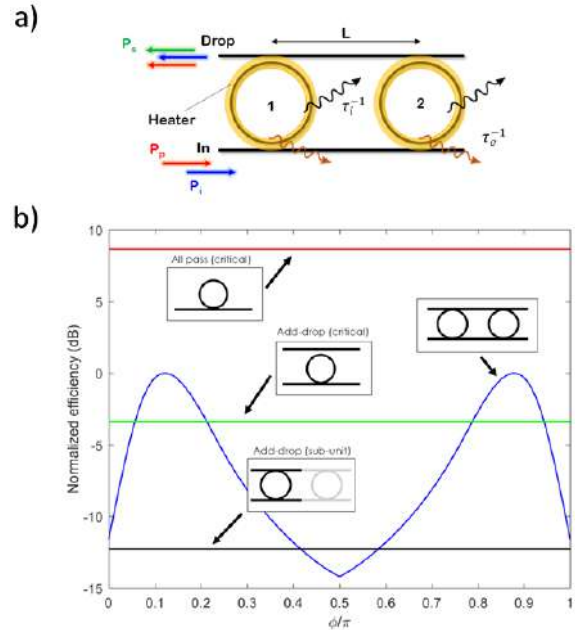


**Figure 9:** (a) The photonic molecule. Two ring resonators, labelled 1 and 2, are separated by a distance  $L = 53.01 \mu\text{m}$  and indirectly coupled by two bus waveguides. The resonators have a radius of  $6.5 \mu\text{m}$ , intrinsic photon lifetime  $\tau_i = 250 \text{ ps}$  and extrinsic (associated to an energy decay in the waveguide) photon lifetime  $\tau_e = 75 \text{ ps}$ . (b) The FWM conversion efficiency of the photonic molecule (blue curve), as a function of the inter resonator phase  $\phi$ , is compared to the one of the critically coupled All-Pass (red curve) and Add-Drop (green curve) resonators, and to the one of the Add-Drop resonators which form the molecule (black curve). The maximum of the conversion efficiency of the photonic molecule has been set to zero, and all the curves are referred to this level.

The possibility to shape and localize the electric field inside the different constituents of the molecule makes them attractive for cavity-enhanced nonlinear optics. We studied the coherent control of Four Wave Mixing in a molecule made by two indirectly coupled ring resonators on a Silicon nanophotonic chip. As shown in Fig. 9(a), we injected a Pump and a stimulating beam resonantly with ring 2, and we monitored the power of the generated Signal in the parameter space spanned by the inter-resonator phase and eigenfrequency detuning ( $\phi, \Delta\nu$ ). We indirectly observed collective excitations, analogous to sub-radiance and super-radiance of diatomic systems, with a respectively long (hundreds of ps) and short photon lifetime. Sub-irradiance is exploited to enhance the internal field, increasing the FWM signal by a factor of 5 compared to the maximum achievable from the single constituents of the molecule. Remarkably, from the detection of the top scattered light, we also observed molecular states characterized by perfect energy equipartition among the two rings. In these states, FWM is suppressed by the destructive interference of the Signal waves scattered from the two resonators in a common bus waveguide. We then compared the FWM conversion efficiency of the molecule to other geometries which make use of single rings. The comparison is shown in Fig. 9(b). The

molecule, in the sub-irradiant state ( $\phi \sim 0.87\pi$  or  $\phi \sim 0.13\pi$  in Fig. 9(b)) shows a conversion efficiency which greatly exceeds the one of its internal constituents by approximately 12.5 dB, and overcomes also a critically coupled Add-Drop resonator (of same intrinsic quality factor) by 3.5 dB. The performance of the critically coupled All-Pass ring is, however, never exceeded. The photonic molecule, while being superior within the class of the considered four port devices, still remains a sub-optimal configuration if compared to the single bus one. This could be intuitively understood from the fact that our coupling scheme employs two decay channels into the external waveguides, while the single bus configuration only one. However, even if the photonic molecule is an intrinsically sub-optimal configuration for reaching record FWM efficiencies, its internal degrees of freedom allows a level of coherent control of the FWM signal which can not be reached by single bus resonators. As an example of application, fast phase shifters based on carrier-depletion could be used to switch between states where FWM is enhanced or suppressed, acting as a wavelength converter for high speed data communication.

## References

[1] M. Zhang, C. Wang, Y. Hu, A. Shams-Ansari, T. Ren, S. Fan, and M. Lončar, “Electronically programmable photonic molecule”, *Nat. Photonics*, 13 (1), 36, 2019.

## 8. Intermodal FWM (Matteo Finazzo, Stefano Signorini)

Four Wave Mixing (FWM) is a nonlinear third order optical process involving four waves in a  $\chi^{(3)}$  medium. This technique is interesting particularly for wavelength conversion and quantum state generation. In FWM, two pumps wave combine together in order to produce two new harmonics, the signal and the idler waves. The basic requirement for this process to take place is energy conservation; while for an efficient generation a phase matching condition has to be satisfied.

These two conditions together determine the feasibility of the process and the generated wavelengths. The phase matching imposes a strong requirement on the group velocity dispersion of the medium in which the process takes place, which is satisfied in materials with anomalous group velocity dispersion (GVD). With this method, once a careful design has been made, the phase matching condition is usually satisfied only near the pump wavelength, which then introduces the issue of an efficient filtering of the pump itself. Moreover, this limits the allowed conversion range.

Intermodal FWM achieves phase matching exploiting the different dispersion curves characterizing the different waveguide modes. In this way anomalous GVD is no longer required. In addition, this allows a wider range of wavelengths, centred around the pump, in which generation of signal and idler can be achieved. The FWM output wavelengths are now widely tunable working on the waveguide geometry. A price to be paid with respect to the intramodal FWM is the lower efficiency due to a decreased mode field overlap.

In order to obtain excitation of higher order modes, a scheme like the one in Fig. (Fig. 10) can be used.

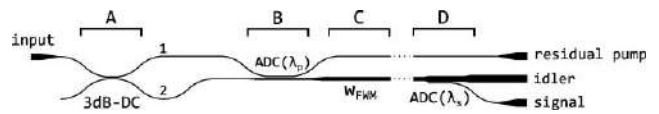


Figure 10: Scheme of the chip

In section A, the pump is split to 50-50 with a directional coupler; in section B there is an asymmetric directional coupler in which one of the two waveguides is multimodal and a higher order mode can be excited. For the present design the high order mode is the second order one. The FWM process takes place with a pump wave on the first order mode and one on the second order mode. The signal wave is generated on the second order mode while the idler is on the first order one. In section D the idler and signal waves are separated using another asymmetric directional coupler. A waveguide with the residual pump helps to characterize the efficiency of the second order mode excitation. A measurement of spontaneous FWM on one chip yields the results shown in Fig. 11.

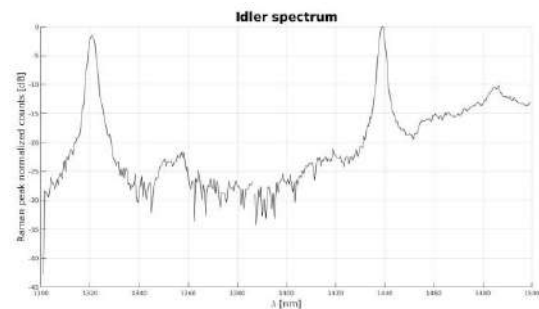


Figure 11: Idler spectrum

Here the pump is at 1550 nm, the idler is generated at 1321 nm, while the signal is at 1875 nm. In the spectrum shown in Fig. 11 only the idler is observed since the signal falls in a spectral region where the InGaAs photodetector is blind. Note a Stokes peak at 1440 nm.

## 9. Broadband and filter-free heralded single photons in silicon waveguides (Stefano Signorini, Sara Piccione, Matteo Finazzo)

In integrated quantum photonics, the source of quantum states of light has to be integrated in the chip, which would enable the fabrication of compact and efficient quantum devices at low costs. Aiming at the creation of a quantum chip in silicon, our research focused on the application of spontaneous four wave mixing (SFWM) to the generation of heralded single photons (HSPs). Up to now, the generation of high purity HSPs through SFWM was based on the narrow spectral filtering of the idler and signal beams, reducing the multimode character of the emission at the expenses of the brightness and scalability of the source.

In this work, we want to get rid of the spectral filters for the generation of HSPs exploiting the properties of the intermodal FWM in waveguide. We have recently demonstrated the intermodal FWM in silicon waveguides, with discrete band phase matching and with unprecedented spectral distance between the generated photons. The discrete nature of the phase matched bands acts as a filter for the generated photons, enabling an easier purification of the heralded single photon state. At the same time, the large and easy control of the signal and idler bands allows designing HSP sources with high purity and brightness, far from the pump and Raman noise. Therefore, we designed an integrated chip which exploits an intermodal combination with the pump (1550 nm) on both the first and second transverse electric (TE) modes, the signal (1909 nm) on the second TE mode and the idler (1304.5 nm) on the first TE mode. The signal is detected by means of an up-converter system able to detect the mid infrared light at room temperature.

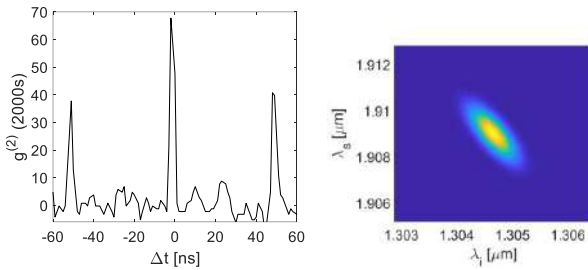


**Figure 12:** a) Measured  $g^{(2)}$  for the signal at 1909 nm, with 3W peak pump power, 40 ps pulse width and 20 MHz repetition rate. b) Simulated JSA for the experimental case in a, showing the reduction of the multimode emission

We want to use the idler as the herald and the signal as the heralded photon, demonstrating the first HSP source without spectral filtering and with broad band generation in silicon waveguides. The first measurements yielded a coincidence to accidental ratio (CAR) of about 7.7 with a purity of 0.66, as measured from the unheralded  $g^{(2)}$  in Fig. 12(a). Thanks to the tunability of the phase matched bands offered by the intermodal approach, the joint spectral amplitude (JSA) can be engineered by simply changing the pump bandwidth or the waveguide geometry, with purities exceeding 0.85 also for single photons above 2 μm. Fig. 12(b) shows the simulated JSA corresponding to the experimental measurement in Fig. 12(a); this JSA it is not yet optimized, but the reduced multimode emission is already visible.

The intermodal HSP source can be a promising candidate for the development of integrated sources of quantum light with low noise, tunable generation, high purities and in the mid infrared (MIR) part of the spectrum. This, in particular, is of great interest for the developing field of integrated quantum sensing in the MIR range.

## 10. Cavity ring down spectroscopy (Andrea Volpini, Stefano Biasi, Pierre Guilleme, Giorgio Fontana)

Microresonators are one of the most important building

blocks of integrated photonics. Their light storage capacity is given by the quality factor (Q). Several techniques have been proposed to measure Q: from the simple measurement of the frequency transmission response to more complex cavity-ring-down spectroscopy. Here we propose to determine Q by measuring the time response of a microring to a rectangular pulse. This allows describing the physics of the system by means of a simple analytical model. In fact, considering the temporal coupled mode theory and making use of the Faltung theorem, one can express the output electric field as the convolution between a Green's function and the input field.

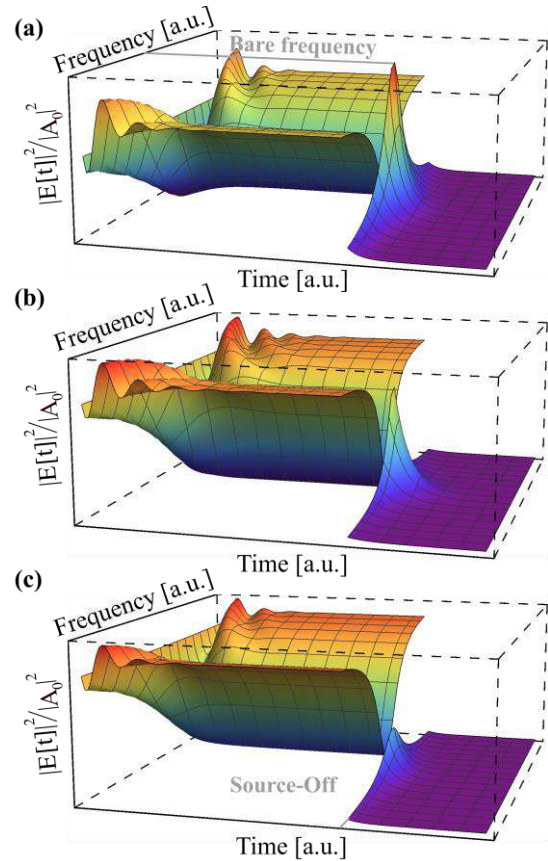


**Figure 13.** (a)-(c) Square of the electric field as a function of the time and frequency. (a) Over-, (b) critical- and (c) under-coupling regime.

Fig. 13 shows a 3D plot of the output electric field as a function of the time and frequency for the three different coupling regimes of a microring resonator: over-, critical- and under-coupling (panel (a), (b) and (c) respectively). In the first part of the three panels, the magnitude of the output electric field decreases for increasing time until the system reaches the stationary regime. When the source is turn-off the resonator discharges the trapped power with an exponential law whose time constant depends on the microring cavity factor. The resonance wavelength is indicated by the frequency maximum of the microring discharge peak. Measurements performed with this method on a  $\text{Si}_3\text{N}_4$  microring resonator monolithically integrated in a silicon chip yields a quality factor  $Q = (5.74 \pm 0.01) 10^5$  at 1064 nm.

## 11. Doublet peak unveiled (Stefano Biasi)

One remaining loss mechanism in high or ultra-high quality factor microresonators is the backscattering created by surface roughness. Its presence is observed as a characteristic mode-splitting in the optical transmission responses that reveals the presence of co-propagating and counter-propagating modes. Typically, the stochastic nature of the roughness introduces a simple statistical averaging that leads, on average, to a symmetric backscattering. This phenomenon is explained by considering a Hermitian coupling coefficient related to the conservative exchange of energy between counter-propagating-modes.

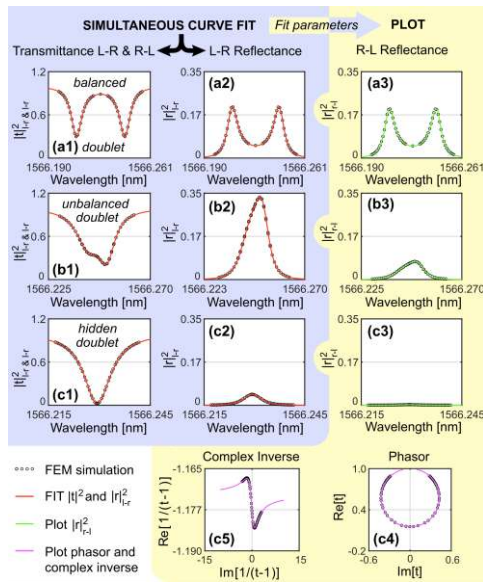


**Figure 14.** Transmission (a1-c1),  $l$ -r (a2-c2) and  $r$ -l (a3-c3) reflections for different realizations of the disorder which yield a balanced doublet (1), an unbalanced doublet (2) and a hidden doublet (3). The black circles are the simulation values while the red line is the fit with the theory.

On the contrary, we showed that the multiple back-scattering processes on the surface roughness in a multi-modal-resonator is not enough to neglect the possible asymmetric behavior of the scatterers. Introducing analysis methods based on phase measurements (parametric phasor and inverse complex representation), we demonstrated that the roughness could exhibit a collective “non-symmetrical” behavior and, thus, asymmetrical reflectance spectra. The idea is that the symmetrical losses, depending on the propagation direction of the beam, could be differently distributed between conservative and dissipative couplings. Therefore, the known coupling equations should be generalized by introducing non-Hermitian coupling coefficients.

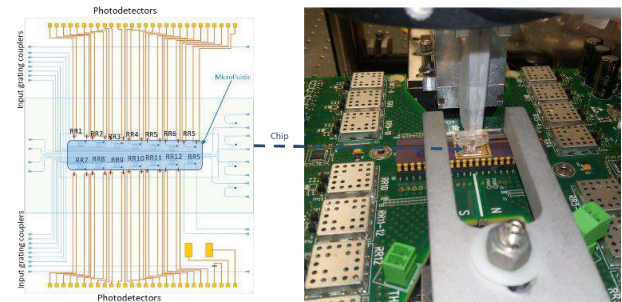
In the non-Hermitian systems, whereas the Lorentz reciprocity theorem enforces equal transmission in both directions, the reflection can be completely different. This is not the case of the Hermitian systems, where the equal transmission also requires equal reflection.

Fig 14 shows the numerical results and the analytical fit for different realizations of the disorder which yield the three

possible scenarios: balanced, unbalanced and hidden doublet (panels (a), (b) and (c) respectively). The formation of these three cases is strictly connected to the non-conservative nature of the coupling coefficient, which can introduce different values of the reflection in the two directions. The non-Hermitian nature of the system can lead, in the limit case, to the scenario where there is a maximum contrast between the amplitudes of reflection in the two directions (see panels (c) of Fig. 14). Formally, this occurs in non-Hermitian systems when the conditions of exceptional points are met. As a result, the two eigenvalues and their eigenvector simultaneously coalesce and become degenerate. Consequently, there is no longer a doublet and the amplitude of the reflection is maximum in one direction and is reduced to zero in the other.

## 12. Si<sub>3</sub>N<sub>4</sub> microring resonators for Thrombin sensing (Tatevik Chalyan, Giorgio Fontana)

In an industrial project, we tested integrated microring resonator (MRR) biosensors for comprehensive analyses of Thrombin. Si<sub>3</sub>N<sub>4</sub> MRRs with 40  $\mu\text{m}$  radius were fabricated in ST Microelectronics. On a single chip 14 MRRs are present (see Fig. 15). In the testing set-up, a JDS Uniphase CQF975/708 series tunable laser, 1530 nm central wavelength, is coupled to the waveguides through grating couplers. The MRR transmitted signal is detected by integrated photodetectors. For the signal readout a PCB board produced by Femtorays is used (see Fig. 15).



**Figure 15:** (Left) MRR chip design. (Right) the chip is placed on the PCB board. A microfluidic made from PDMS is aligned on the top of the chip (blue rectangular on the left image).

In order to define the performances of the MRRs from bio-sensing prospective, we characterize the bulk Sensitivity ( $S$ ) and the Limit of Detection (LOD) of the uncovered MRR5. For this particular MRR, the output signal is collected with a fiber through a grating coupler. The value of the Q-factor for the MRR5 from different chips is measured to be  $16000 \pm 3000$ . To determine the bulk sensitivity, we monitored in real-time the resonance wavelength shift while the sensor was exposed to glucose-water solutions of various concentrations. The refractive index of such solutions is calculated empirically by using glucose concentrations. Fig. 16 shows the results where a bulk sensitivity of 1500 pm/RIU is obtained.

Finally, Thrombin sensing measurements are performed when the MRRs are functionalized by aptamers. Fig. 16(c)

shows the sensorgram of 10 nM Thrombin biosensing measurement. MRR6 with  $Q=18000$  is used in this case. 5  $\mu\text{L}/\text{min}$  flow rate is applied in continuous flow method. The measurement starts at  $t=0$  minute with flowing a buffer solution. Next, at  $t=3$  minute, 10 nM Thrombin is injected to the sensor surface and a resonance shift of 9 pm wavelength is observed thanks to Thrombin binding to the aptamers.

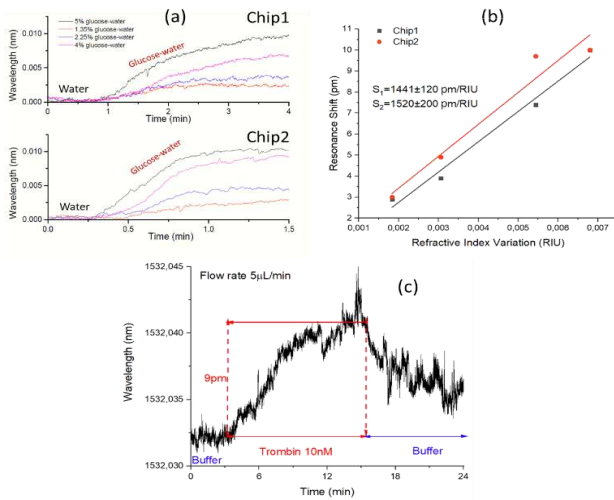


**Figure 16:** Biosensing measurements. (a) Wavelength shifts obtained with MRR5 during the injection of the water-glucose solutions. (b) Evaluation of the bulk sensitivity. (c) 10 nM Thrombin measurement.

At  $t=15$  minute, the sensor is rinsed with buffer and we observe a decrease of the signal with a remaining shift of few pm which shows the chemical binding of the Thrombin to the aptamers. These preliminary results allow concluding that the MRRs functionalized by aptamers can be used for biosensing applications and by further improvement of the LOD it is possible to yield sensors comparable to the state of the art.

### 13. Optimization of the IRIS chip (Astghik Chalyan, Stefano Tondini, Giorgio Fontana, Manuel Alessandro Medina, Claudio Castellan)

In the European IRIS project (Integrated Reconfigurable Silicon photonic Switch) a wavelength selective switch matrix was designed, fabricated and tested. The chip architecture is shown in Fig. 17. The IRIS optical switch has 4 network ports (NP1-NP4) and 8 local ports (LP1-LP8). In one transmission direction, the various wavelength signals coming from the four network fibers are distributed to the eight local ports and, in the opposite direction, the wavelength signals from the eight local ports are injected into the network fibers.

We applied a stochastic optimization algorithm based on the Globalized Bounded Nelder-Mead (GBNM) method to align the spectral response of each component to the ITU grid. The first component which we aligned was the interleaver. The target function that the algorithm aims to maximize is the optical power transferred into one arm of the interleaver. We exploit the thermo-optic effect to shift the

interleavers pass-band in a desired spectral position. The interleavers are provided with dedicated metallic heaters that can be operated in order to tune the interleaver response, which is typically misaligned due to fabrication inaccuracies. The experimental setup, which is shown in Fig. 18, is made of a tunable laser coupled with one input port of the optical switch, while the transmission at the output was recorded with an InGaAs detector.

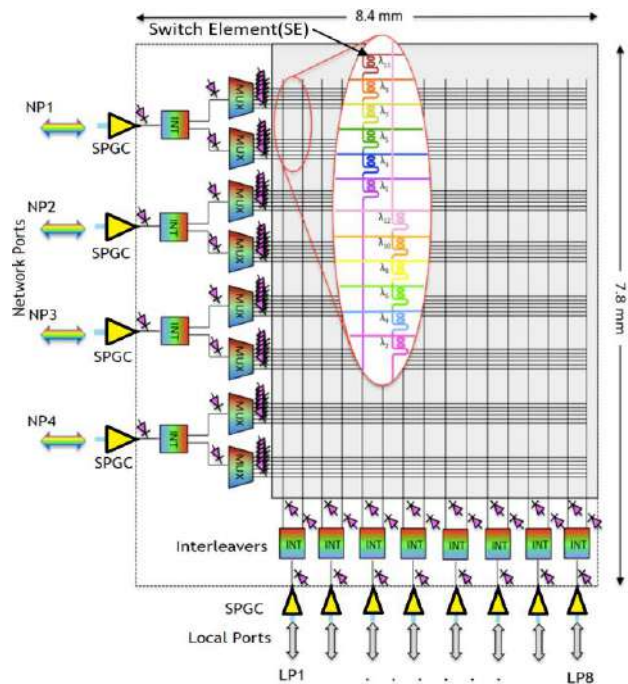


**Figure 17.** IRIS switch architecture

The optimization algorithm is implemented via a software to drive the analog electronic circuit which provides the current to the integrated heaters. The software finds the best heating configuration (on the two branches of the interleaver) on the basis of a feedback loop where integrated monitor diodes are used. This way, the even and odd wavelengths input in the interleaver are directed toward the wanted lines within the switching matrix.

This method has been used also to align the micro-ring switching elements. In this case, the control enables different pathways for the routing or the broadcasting operation of the optical switch. With no bias applied to the heaters of the switching elements, the optical signal is expected to be maximum at the through port. When the micro-ring heaters are biased, the feedback controller finds the best set of heating values that minimize the optical power at the through port of the switching node. This way, the optical signal is coupled in the drop port and the node is enabled for switching.

The calibration procedure allows determining the optimal working condition for each component, i.e. the voltages/currents needed to trim its characteristics to the desired value. All the information collected during the calibration are stored in a look-up-table (LUT) that can be used to set up the wanted switching configuration or to restore the de-

fault position of the switch elements. The algorithm, implemented in LabVIEW, converges over multiple instances and it is robust against stagnation. This work demonstrates the automatic reconfiguration/restoration of the whole optical switch.



Figure 18: Experimental setup

#### 14. Photonic-based feed-forward neural networks (Davide Bazzanella, Enver Sangineto, Paolo Bettotti, Giovanni Donati)

Recently, Artificial Neural Networks (ANNs) have become gradually more accessible and tackle problems of increasing complexity, leading to dramatic improvements in Artificial Intelligence. The drive to increase the efficiency of the ANN computation operations is very strong. Usually, ANNs are run on standard (von Neumann-based) computers, in which the CPU is accelerated by ASICs (GPUs). However, new computational architectures can potentially largely speed-up the ANN processing time.

This motivates our investigation; we focus on the advantages of silicon photonics in order to build a new architecture which can efficiently execute ANN tasks. Specifically, using integrated photonics structures, we aim to develop a Feed-Forward Neural Network architecture where we physically implement one of the most critical ANN components: the "activation function".

The physical device which performs the activation function is a single microring resonator in the Add-Drop Filter configuration (ADF). In this configuration, the microring is coupled with two waveguides in order to inject and extract the light signal. We characterized its (thermal) nonlinear response (Fig. 19), which will be used as the activation function.

An important part of this work was the software-based simulation of our photonic ANN, using PyTorch, an open-source software library for the development of ANNs, and the MNIST dataset, a common benchmark for the ANN research community. This simulation is important for two reasons: (1) The photonic ANN training (weight setup) and (2) The comparison of the performance of standard ANNs with the performance of our simulated photonic ANN. Specifi-

cally, the training part cannot be done directly on the photonic circuit and needs to be computed using a software simulation. Moreover, while training the network, we need to balance the final network accuracy with the constraints related to the photonic implementation. In more detail, the ANN weights need to satisfy these constraints: (a) They should all be positive; (b) They have to sum up to 1 in order to conserve the energy exiting from a given neuron.

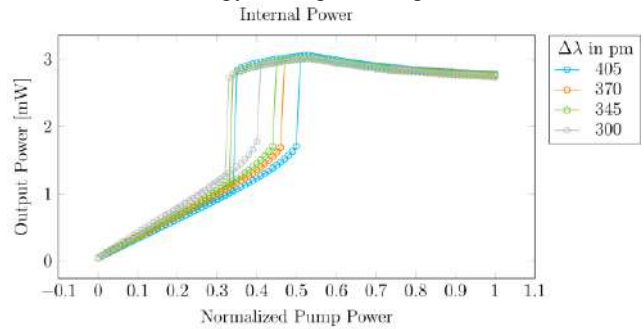


Figure 19: Nonlinear response of the microring resonator due to the thermal bistability. The output power vs. the normalized input power is reported for few values of the wavelength detuning of the input signal from the microring resonance.

We solved this constrained-optimization problem using a technique called Projected Gradient Descent, in which the Gradient Descent approach, commonly used for ANN training, has been modified introducing iterative projections of the network's weight vector into the admissible area defined by our constraints. Finally, using MNIST, we compared our simulation results with standard, non-constrained ANNs, achieving a similar performance.

#### 15. Optogenetics and neurons (Clara Zaccaria)

Here, the idea is to realize a hybrid neuromorphic computing platform in which integrated photonic circuits and a neuronal network are able to compute jointly, in order to emulate brain processes and develop schemes able to supplement neuronal functions. The photonic circuit and the biological system will communicate through optogenetics: neurons will be transfected with DNA constructs expressing channel-rhodopsins (ChRs), photosensible proteins which act like ionic channels on the cell's membrane.

These rhodopsins are composed by a retinal chromophore that detects light and a protein called opsin, bounded together covalently. Upon absorption of a photon, the retinal isomerizes and triggers a sequence of conformational changes within the opsin partner [1]. The whole rhodopsin is located across the cell's membrane and acts like an ionic channel: the photoinduced structural rearrangements of the protein correspond to the opening – or closing – of the channel.

This means that it is possible to excite or inhibit neuronal activity simply by illuminating the infected regions of the cells (Fig. 20).

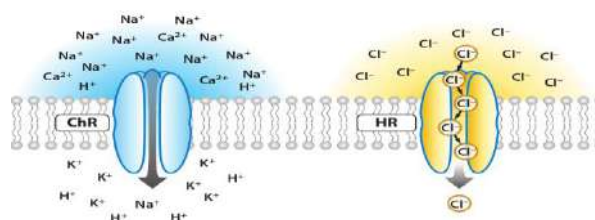


**Figure 20:** Two examples of Optogenetic Proteins: Channelrhodopsins when activated with blue light conduct cations and induce an action potential; Halorhodopsins instead inhibit neurons after illumination with yellow light.

The best known channelrhodopsins can be activated in the visible spectrum, in particular in the blue-green range: the most red-shifted protein synthesized is activated at around 600 nm [2].

The first part of the project will consist in growing infected embryonic E17 cortical neurons on a photonic chip and in studying their response to light. Along the photonic circuit there will be some scattering points which will allow the stimulation of the infected neurons located over that specific sites. The electric activity of neurons will be detected using a fixed electrode configuration that acts like a multi electrode array integrated directly in the photonic circuit.

## References

- [1] L. Fenno, O. Yizhar, K. Deisseroth, The Development and Application of Optogenetics, *Annu. Rev. Neurosci.* 2011. 34:389-412
- [2] K. Oda, J. Vierock, S. Oishi et al. Crystal structure of the red light-activated channelrhodopsin Chrimson, *Nature Communications* (2018) 9:3949

## 16. Nanocellulose hydrogels as carrier for drug delivery applications

(Chiara Piotta, Paolo Bettotti)

Nanocellulose (NC) is a fascinating material obtained by disrupting cellulose fibers down to their elementary, crystalline building blocks. These tiny elongated crystals can be arranged into different forms to produce smart materials. Currently, we are investigating the use of NC hydrogels as carrier for drug delivery applications. Hydrogels are formed by ionotropic gelation dropping concentrated solutions of NC crystals in saline buffers. Their mechanical properties are varied by playing with the crosslinkers used to “freeze” the nanocrystals and allow the preparation of gels with tunable stiffness. Obviously, mechanical properties reflect into altered diffusivity of the drugs loaded within the gel.

Since about 40% of the new pharmaceutically active compounds are hydrophobic, there is the need to develop efficient systems to deliver and protect them from degradation, while keeping the highest bioavailability.

Our research in this field have considered two highly hydrophobic molecules as model drugs: beta-carotene (BC) and clofazimine (CFZ). The former has been chosen for its non-

polar structure and ease of degradation (it is a natural anti-oxidant); while the latter is a poorly soluble molecule that brings polar functional groups. The structural differences among these two molecules help to clarify how they do interact with the environments in which they are trapped.

CFZ has a complex spectral response as it heavily interacts with ions. Its spectral shape changes during the release and shows a clear isosbestic point (see Fig. 21).

Release kinetics show typical saturation curves that do not follow a Fickian diffusion, probably because structural and mechanical modification of the gel beads modify the diffusivity during the release.

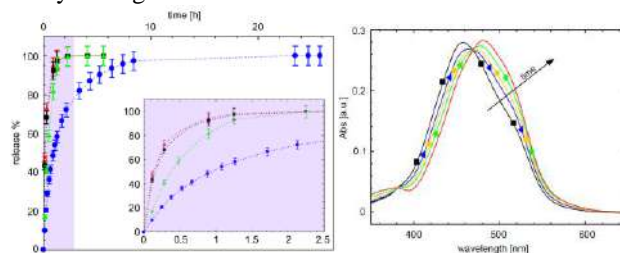


**Figure 21** (a) spectral modification of the CFZ during the release due to the different solvation of the molecule; (b) release curve for hydrogels loaded with different amount of CFZ. The inset is a zoomed view of the first 2.5 hours.

It is worth to note that, in hydrogels co-loaded with proper surfactants, we increased the CFZ water solubility by about 53 times.

## 17. Gain saturation dynamics in Semiconductor Optical Amplifier (Sara Piccione)

Semiconductor, or diode, lasers are playing an increasingly important role in optics, thanks to several advantages with respects to other type of laser. For example, they exhibit one of the highest conversion efficiency with respect to other technology with the need of a simpler power supply and cooling system. Moreover, they show a high reliability at a low cost and at a small size, making more feasible the realization of integrated sources. A laser comprises two essential elements: a coherent optical amplifier, which initiates the light emission and an optical resonator acting as a feedback system, which maintains the laser oscillation. Therefore, fundamental in the understanding of the laser behavior is the knowledge of the gain of the amplifier. This is defined by the increased number of photon per unit area per unit time which can be expressed by

$$\frac{d\Phi(z)}{dz} = \gamma(\nu)\Phi(z) \quad (1)$$

where  $\gamma(\nu)$  represents the net gain of the photon flux per unit length of the amplifying medium. The solution of (1) is an exponentially increasing function and, for an interaction region of length  $d$ , the overall gain is defined

$$G = e^{\gamma(\nu)d} \quad (2)$$

However, in the real scenario the solution is not so easy since the population inversion, to which the gain is linked, depends on the initial photon flux. To find the correct value of the gain we need to solve the rate equations, which describe the rates of change of the population density in each of the energy state involved in the transition.

Under steady state condition the solution lead to the following expression

$$\gamma(\nu) = \frac{\gamma_0(\nu)}{1 + \Phi/\Phi_s} \quad (3)$$

where  $\gamma_0$  is the small-signal gain, while  $\Phi_s$  the saturation photon flux. The dependence of the gain on the photon flux, which can be found by substituting (3) into (1) and integrating for the total length of the active medium, can only be obtained numerically.

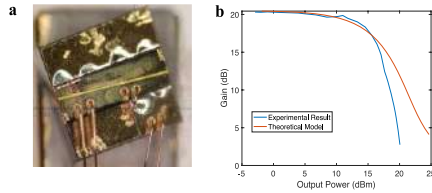


**Figure 22:** a) Top view of the amplifier chip. b) Comparison between the experimental results and the theoretical model.

Fig. 22 (a) shows a top view of the semiconductor optical amplifier (SOA) chip which we are characterizing within an industrial project. The yellow line on the top is the portion of the active medium where the amplified signal is guided through the amplifier. The input signal, coming from an external laser source at a wavelength of  $\lambda=1550$  nm is coupled to the amplifier chip thanks to a focusing lens. At the output of the amplifier light is collected thanks to the use of a collimating lens. The output light contains both the contribution of the amplified signal and that of the signal spontaneously emitted from the amplifier, or ASE.

In figure 22 (b) the blue curve indicates gain as a function of the power at the output of the amplifier, when the injected current is equal to  $i=500$ mA. On the other hand, the red curve instead shows the theoretical prediction given by eq. (3).

For small values of the output power, or equivalently of input power, the experimental curve resembles pretty well the theoretical model. However, as soon as the output power increases, the saturation dynamics, experimentally measured, changes notably from the theoretical prediction. The reason is attributed to the nonlinear process of two-photon-absorption (TPA), whose extent is related to the imaginary part of the third-order nonlinear susceptibility of the material.

The main difference from linear absorption is the dependence of TPA on the light intensity. For this reason, at high intensities the nonlinear process can dominate over the linear absorption. TPA has long been known to limit the optical intensity transmitted through a semiconductor waveguide, but due to the high intensities required to produce it, the effect happens with a higher probability under short-

pulses excitation. However, in waveguide devices of small dimension, as in our case, TPA can be present and significant limits the circulating power also in CW operation. TPA introduces both primary and secondary optical loss mechanisms to the propagation of optical signal through a semiconductor waveguide. The primary mechanism is the direct depletion of the optical field due to the absorption of the two photons. The secondary loss mechanism results from free-carrier absorption (FCA) associated with TPA generated carriers. More in details, the nonlinear absorption process creates equal densities of electrons and holes that recombine via two-photon excited fluorescence.

Fig. 23 (a) shows the comparison between the experimental data and the theoretical model corrected to include the contribution of TPA, while Fig. 23 (b) shows the laser output as a function of the output coupler reflectivity for the two different theoretical models used to describe the gain.

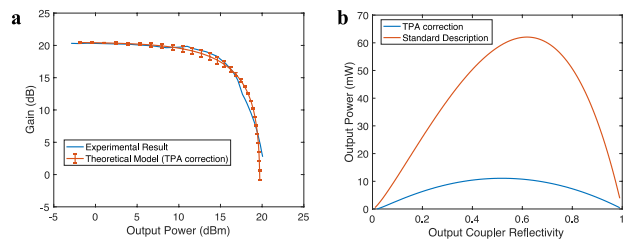


**Figure 23:** a) Comparison between the experimental curve and the theoretical model corrected for TPA effects. b) Laser output power for both the two gain description.

The differences between the two curves highlight how the proper knowledge of the gain behavior is necessary for the modeling of a laser source and to predict the final laser output power.

## 18. Sensor characterization for a smart kitchen environment (Damiano Lodi)

In recent years, the Internet of Things (IoT) has drawn a lot of attention as one of the most promising emerging technology. Its range of applications is extremely various and includes environmental monitoring, industrial automation, building automation, smart agriculture and so on. In general, IoT describes a network of embedded devices with Internet connectivity that allows them to interact and share data with services and people on a global scale. This can improve systems efficiency, reliability and sustainability. The positive reach of smart devices from the consumers and the awareness of the benefits of this technology in industrial applications are pushing industries to research new features for smart devices that can monitor all sort of different parameters. One of the most developing markets is the so-called 'Building 4.0', whose target is to monitor not only the energy efficiency and structural quality of new buildings but also the maintenance of the wellness of the living environment.

One of the most important rooms in everyone home is the kitchen, where the social life of the family takes place. Unfortunately, the kitchen environment can also be one of the least healthy, due to all the organic compounds released by

food while cooking. For this reason, in recent years a great effort has been applied in monitoring such environment, but unfortunately with poor success.

The reasons for this failure are different. One of them can be the absence of a standardized parameter to monitor life quality; CO<sub>2</sub> monitoring is not enough, and Volatile Organic Compounds (VOC) regulations can vary highly in different countries. Moreover, all the VOC and gas sensors commercially available today are rather generic and cannot be used to detect specific chemicals. This makes them particularly liable to false positive, which upsets the final consumer and, in turn, decreases the usage and effectiveness of the monitoring device.

The aim of my research, carried out within a local company, is to determine the least possible amount of parameters to describe efficiently the healthiness level in the kitchen environment. To do this, we first need to understand which are the main parameters worth monitoring, and from those, determine only the ones that have the greatest signal variation when a different concentration of pollutants is present. One of the major constraints we are facing is the target price that the final device needs to respect, and this will probably reduce the choice to a maximum of three parameters.

To overcome this constraint, a great effort is placed in the signal analysis with a custom algorithm that will take into consideration various room design and device placement. This will reduce the possibility of a false positive alarm and it will secure a high level of customization for the final customer.

### 19. Cellulose-based Nanomaterials: Structure and Properties (Cecilia Ada Maestri, Marina Scarpa)

Biological materials such as wood show outstanding properties due to the self-assembly of components from molecular to macroscopic size. An emerging nanotechnology-based strategy consists of the isolation of biological components with size in the range from nanometers to micrometers and of the design of human-driven assembly processes to obtain multifunctional materials.

In our lab, we isolate cellulose nanocrystals, with dimensions of around 4-5 nm in width and some hundred nanometers in length, and investigate their assembly processes through weak interactions among them and with small molecules, like water or ions. In particular, we focus on cellulose nanocrystals supramolecular self-organization both in absence and presence of water, studying cellulose nanocrystals-based films and hydrogels.

In dry conditions, cellulose nanocrystals form densely-packed, few micrometers thick films, which provide impermeable barriers for the transport of gaseous molecules such as O<sub>2</sub> and CO<sub>2</sub>.

In aqueous solution, instead, cellulose nanocrystals undergo sonication- or cation-assisted entanglement, forming soft hydrogels. Na<sup>+</sup>, Ca<sup>2+</sup> and Al<sup>3+</sup> crosslink the nanocrystals and produce stable hydrogels with structurally ordered domains

in which water is confined. Since the gelation process is diffusion controlled, small hydrogel objects with different size and shape can be designed knowing the diffusion kinetics.

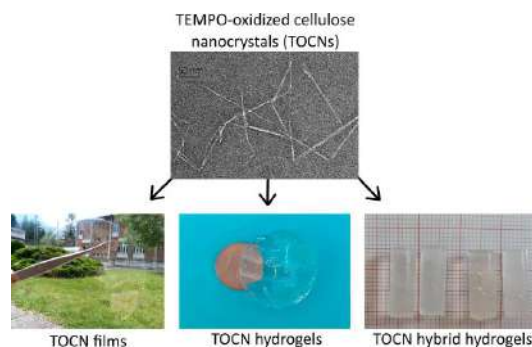


**Figure 24:** TEM microscopy image of Cellulose Nanocrystals and pictures of the nanocellulose-based materials resulting from their self-assembly in different conditions.

In parallel to material characterization, we investigate the possible exploitation of cellulose nanocrystals-based materials in the biomedical field. In this regard, toxicity studies were performed both on the individual nanocrystals and on the films and hydrogels resulting from their assembly. Moreover, we are developing and characterizing a hybrid cellulose-nanocrystals/chitosan material, which shows some potential to be used as therapeutic delivery system in the gastrointestinal tract. Indeed, though a mould assisted gelation process, composite hydrogels can be produced, which are degraded by human digestive enzymes and release a model protein according to a biphasic kinetic profile.

#### For more info

Nanoscience Laboratory  
Department of Physics  
University of Trento  
via Sommarive 14  
38123 Povo- Trento (Italy)  
<http://nanolab.physics.unitn.it/>

secretary dr. Tanya Egorova  
email [tatsiana.egorova@unitn.it](mailto:tatsiana.egorova@unitn.it)  
phone +390 461 283172